DEVELOPMENTAL NEUROSCIENCE

LHX2 regulates dendritic morphogenesis in layer II/III neurons of the neocortex

Mahima Bose[1]†, Sreenath Ravindran[1]†, Sanjna Kumari[2], Achintya Srivastava[1], Archana Iyer[1], Binita Vedak[1], Ishita Talwar[1], Rishikesh Narayanan[2], Shubha Tole[1]*

In the mammalian neocortex, the two hemispheres communicate via the corpus callosum. We investigated mechanisms regulating dendritic arbors and spines of callosal neurons. The transcription factor LIM Homeodomain 2 (*Lhx2*), a key regulator of cortical development, is expressed in postmitotic layer II/III neurons and their progenitors. Loss of *Lhx2* in either population caused similar but distinct phenotypes: reduced dendritic arbors, altered spine morphology, and changed electrophysiological properties. Morphometric defects were more severe when *Lhx2* was disrupted in progenitors and were recapitulated by its specific loss in basal progenitors. *Lhx2* loss in progenitors aberrantly up-regulated *Neurog2* in postmitotic neurons, and *Neurog2* knockdown partially rescued the phenotype. Loss of *Lhx2* at either stage also up-regulated Wnt signaling pathway genes. The mutant phenotype was mimicked by constitutive activation of β-CATENIN in postmitotic neurons. Our findings reveal previously unidentified LHX2-dependent mechanisms of dendritic morphogenesis, highlighting its temporally dynamic and diverse roles in neocortical development.

INTRODUCTION

The functional characteristics of a neuron are critically dependent on its dendritic arborization and complexity (*1*). Disruptions in dendritic morphogenesis underlie neurodevelopmental disorders, including autism spectrum disorder and schizophrenia (*2*, *3*). In the mammalian cerebral cortex, neurons from the superficial pyramidal layer, which occupies layers II/III, broadly extend their apical dendrites into layer I and basal dendrites within their layer. They also establish connections with the contralateral hemisphere via the corpus callosum. These neurons are born relatively late in cortical neurogenesis, with their production peaking at embryonic day (E) 15.5 in the mouse (*4*).

Dendritic morphogenesis is regulated by multiple factors, including transcriptional regulators, guidance cues, cell adhesion molecules, cytoskeletal elements, and neuronal activity (*5*, *6*). Among these, transcription factors are known to drive downstream signaling pathways and gene expression crucial for dendritic development (*7*). In the developing mammalian cerebral cortex, transcription factors such as *Cux1*, *Cux2*, *Zfp312*, and *Foxg1* promote dendritic arborization in specific neuronal subtypes, where the loss of any of these genes results in reduced complexity (*8*–*12*). Conversely, factors like *Sox11*, *Tbr1*, and *Neurog2* suppress excessive branching, such that the loss of these factors leads to increased complexity (*13*–*15*). Some of these factors, e.g., *Zfp312*, *Sox11*, *and Tbr1*, have been shown to exclusively regulate morphometry in specific subtypes of postmitotic neurons (*11*, *14*, *15*), while others, such as *Foxg1*, exhibit a broader expression pattern that encompasses various progenitors and neuronal classes (*12*, *16*). This raises an important question: Is the modulation of dendritic architecture solely a postmitotic event, or do genetic mechanisms in neuronal progenitors presage regulatory control of dendritic morphogenesis that manifests at postmitotic stages?

The transcription factor LHX2 is involved in various aspects of cortical development, including cortical patterning, progenitor proliferation, cell fate decisions, neuron subtype specification, thalamocortical axon guidance, and barrel formation (*17*–*19*). *Lhx2* has been shown to have different roles when deleted from progenitors or postmitotic neurons (*18*). For example, *Lhx2* loss in progenitors disrupts subplate neuron function, leading to premature thalamocortical axon invasion of the cortex, degeneration of sensory thalamic neurons, and the subsequent loss of barrel fields (*17*, *18*). In contrast, the deletion of *Lhx2* in postmitotic neurons does not result in these defects, and axons demonstrate normal waiting behavior at the subplate. This indicates that *Lhx2* functions in progenitors to establish mechanisms that shape neuronal properties during the postmitotic stage (*18*).

Here, we investigated the impact of *Lhx2* loss on the dendritic arborization and spine maturation of upper-layer callosal neurons. We show that loss of *Lhx2*, effective either from the cortical progenitor stage or specifically in postmitotic neurons, causes profound alterations of the dendritic and spine morphology of layer II/III neurons. However, affected neurons retain their callosal identity and send projections to the contralateral hemisphere, indicating that LHX2 has a selective modulatory role in the dendritic morphogenesis of these neurons.

Loss of *Lhx2* from progenitor stages results in aberrant up-regulation of *Neurog2* in postmitotic neurons derived from these progenitors, an effect not seen when loss of *Lhx2* is effective selectively from the postmitotic neurons. The simultaneous knockdown of *Neurog2* can partially rescue the dendritic arborization defects resulting from the loss of *Lhx2*, indicating that *Neurog2* is a key downstream effector of *Lhx2* in dendritic development. In addition, *Lhx2* deletion, whether from the progenitor stage or postmitotic neurons, leads to up-regulation of the Wnt signaling pathway components in postmitotic neurons. We further demonstrate that an independent β-catenin stabilization in postmitotic neurons phenocopies the dendritic and spine morphology defects observed in *Lhx2* postmitotic mutants, suggesting that *Lhx2* regulates postmitotic dendritic architecture, in part, through Wnt signaling. In summary,

[1]Department of Biological Sciences, Tata Institute of Fundamental Research, Mumbai 400005, India. [2]Cellular Neurophysiology Laboratory, Molecular Biophysics Unit, Indian Institute of Science, Bangalore 560012, India.
*Corresponding author. Email: shubhatole@gmail.com
†These authors contributed equally to this work.

our findings reveal novel insights into the roles of transcription factor LHX2 in orchestrating diverse gene networks that govern the dendritic and spine morphogenesis process.

RESULTS

Layer II/III cortical neuronal birth peaks at E15.5 in mice (*4*). LHX2 protein is detected in the cortical progenitors at this stage and persists in its progeny, the postmitotic layer II/III neurons (Fig. 1, A and B). This observation motivated us to compare the effects of loss of *Lhx2*, from the progenitor stage E15.5 or the newborn postmitotic neuron stage, on the dendritic morphogenesis of mature layer II/III neurons. All dendritic arbor and spine morphology measurements were performed on postnatal day (P) 30 in the somatosensory cortex layer II/III. To label the dendritic arbors, we used in utero electroporation (IUE) to introduce a plasmid expressing membrane-bound enhanced green fluorescent protein (CAAX-EGFP) into E15.5 progenitors so that the neurons arising from these cells were labeled in perpetuity (Fig. 1, C and C'). We used an *Lhx2* $^{lox/lox}$ mouse line to affect the conditional loss of *Lhx2*. To disrupt *Lhx2* from the progenitor stage, we co-electroporated a plasmid encoding Cre-TdTomato with CAAX-EGFP at E15.5. For control electroporation, TdTomato (lacking Cre) was used. Postmitotic neuron–specific disruption of *Lhx2* was affected by crossing the *Lhx2* $^{lox/lox}$ line to a line expressing *Neurod6*-Cre [NexCre; (*20*)]. Previous work using this line to disrupt *Lhx2* reported undetectable LHX2 protein in newborn postmitotic neurons at E14.5, during their migration through the intermediate zone and in the cortical plate (*21*). IUE of CAAX-EGFP at E15.5 produced EGFP-labeled layer II/III neurons, which experienced *Lhx2* gene disruption upon becoming postmitotic due to the action of NexCre.

Disrupting *Lhx2* from E15.5 progenitors and newly postmitotic neurons causes dendritic and spine morphology defects in P30 layer II/III neurons

To analyze the fully developed dendritic arborization of layer II/III neurons, we examined CAAX-EGFP–labeled cells at P30 when dendritic morphogenesis was complete. Control neurons displayed a typical layer II/III pyramidal morphology (Fig. 1, C' and D).

In contrast, neurons that lost *Lhx2* from either progenitor (Pg; Fig. 1D') or postmitotic (Pm) stages (Fig. 1D") displayed shrunken dendritic arbors. The total length of apical and basal dendrites was significantly reduced in Pg and Pm mutants, with a more pronounced effect seen in Pg mutants than in Pm mutants (Fig. 1, E and F). The mean length of the basal dendrites exhibited a severe reduction in both Pg and Pm perturbations (Fig. 1G). Sholl analysis of apical and basal dendrites reflected decreased branching complexity in both Pg and Pm mutant neurons. However, this effect was significantly stronger in Pg mutants than in Pm mutants in both apical and basal dendrites (Fig. 1, H and I, and fig. S1). These deficits were broadly recapitulated when electroporated progenitors at E15.5 were isolated in vitro and maintained for 15 days. This indicated that the role of LHX2 is cell autonomous [fig. S2, A to H; (*22*–*24*)].

Disrupting *Lhx2* in E15.5 progenitors and postmitotic neurons causes spine development defects in layer II/III neurons

Dendritic spines serve as the functional units of dendrites and are the sites of synaptic transduction (*22*, *25*). Understandably, the molecular factors influencing dendritic development overlap with those involved in spine development (*22*–*24*). We investigated whether the loss of *Lhx2* from either progenitor or postmitotic stages affects the formation of spines in P30 layer II/III neuronal dendrites. Control, Pg, and Pm mutant neurons were analyzed for spine morphology in apical and basal dendrites. Spines were categorized into filopodial, thin, stubby, and mushroom types, which correlate with the overall maturation stage of the spines (*22*). We observed a significant increase in the percentage of thin spines and a corresponding decrease in mushroom spines in the apical and basal dendrites of both Pg and Pm mutants (Fig. 1, J to S). Stubby spines were significantly fewer in Pm but not in Pg mutant apical dendrites (Fig. 1, M and Q). These findings indicate that LHX2 also regulates the morphogenesis of dendritic spines during neurodevelopment to achieve the mushroom shape typical of mature spines.

Loss of *Lhx2* increases the firing rate and excitability of layer II/III neurons

Dendrites and spines of the neurons are critical for regulating the functional properties of the neurons. We sought to examine the consequences of the morphometric deficits resulting from the loss of *Lhx2* on the electrophysiological properties of these neocortical layer II/III pyramidal neurons. We measured several sub- and suprathreshold intrinsic physiological properties from brain slices of Pg and Pm *Lhx2* mutant neurons using patch-clamp electrophysiology and compared them with their respective controls (Fig. 2 and figs. S3 to S7). Dendritic arborization is a well-established factor in regulating neuronal excitability (*26*, *27*); therefore, we first measured input resistance, a subthreshold measure of neuronal gain. Consistent with the more pronounced reduction in dendritic arbor in Pg *Lhx2* mutant neurons (Fig. 1), we found a significant increase in the input resistance values in this condition compared to their control values (Fig. 2, A and B). However, control and Pm *Lhx2* mutant neurons manifested comparable input resistance values (Fig. 2, C and D). Consistently, impedance amplitude, another measure of subthreshold excitability, was significantly higher than controls in Pg mutant neurons but was comparable to controls in Pm mutant neurons (figs. S3 and S4). Other physiological measurements of subthreshold excitability were also comparable in Pg and Pm mutant neurons compared to their respective controls (figs. S3 and S4).

In contrast, we found both Pg (Fig. 2, E and F) and Pm mutant neurons (Fig. 2, G and H) to manifest significantly higher suprathreshold excitability than in controls. Specifically, we found significantly higher firing frequencies (Fig. 2, E to H, and fig. S5) and a switch to depolarization-induced block with low-current injections (fig. S5, C and D). In addition, Pm mutant neurons displayed a significant reduction in both the latency to the first spike (fig. S6), the first interspike interval (fig. S6), and a significant increase in the peak dV/dt associated with the action potentials (fig. S6). These measurements were not significantly different between Pg mutant neurons and their controls (fig. S7). In summary, loss of *Lhx2* at the Pg or Pm stage resulted in distinct effects on specific electrophysiological measurements, but in both conditions, there was significant enhancement in the action potential firing rate in layer II/III neocortical pyramidal neurons (Fig. 2 and figs. S3 to S7).

Multiple features of upper layer identity are unaffected upon loss of *Lhx2*

The changes in the dendritic morphometry, spine, and electrophysiological properties of these neurons could also be a result of an altered

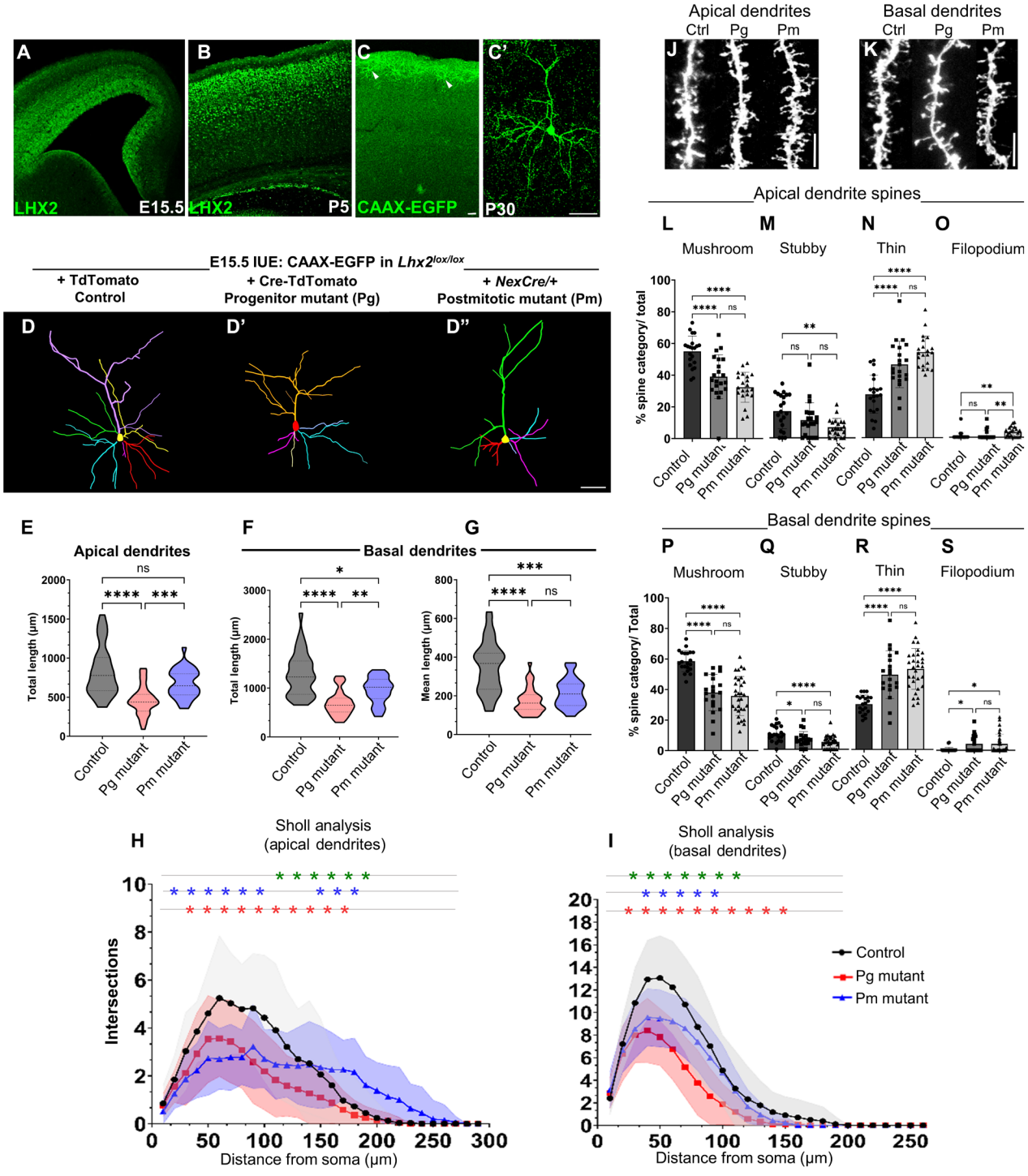

Fig. 1. Loss of *Lhx2* either in progenitors or newborn postmitotic neurons induces dendritic morphology and dendritic spine defects in layer II/III neocortical neurons. (**A** and **B**) LHX2 in progenitors at E15.5 (A) and layer II/III cortical neurons at P5 (B). (**C** and **C'**) A P30 layer II/III neuron labeled by CAAX-EGFP IUE in E15.5 progenitors (**D** to **D"**) Neurolucida tracings at P30. (**E** to **G**) The total length of apical dendrites (E) is significantly reduced in Pg mutants. The total length (F) and mean length (G) of basal dendrites (F) are significantly reduced for Pg and Pm mutant neurons. (**H** and **I**) Sholl analysis of apical dendrites (H) and basal dendrites (I) shows a significant decrease in complexity in Pg and Pm mutants. Thirty-five to 40 neurons were scored for each condition obtained from four biologically independent replicates; Statistical test: Two-way analysis of variance (ANOVA) multiple comparisons with Tukey's correction for Sholl analysis and Kruskal-Wallis test for total/mean length analysis; asterisks indicate pairwise comparisons between control versus Pg mutant (red), control versus Pm mutant (blue), and Pg mutant versus Pm mutant (green). Detailed statistical significance values per intersection row are provided in fig. S1 and data S1. (**J** to **S**) Dendritic spine morphology is affected in Pg and Pm mutant neurons (20 dendrites with 25 spines each were analyzed from each category. Statistical test: Kruskal-Wallis test). For (E) to (G) and (L) to (S), $*P < 0.05$, $**P < 0.01$, $***P < 0.001$, and $****P < 0.0001$. Scale bars in (C) to (C') and (D) to (D") are 50 µm, and in (J) and (K) are 5 µm.

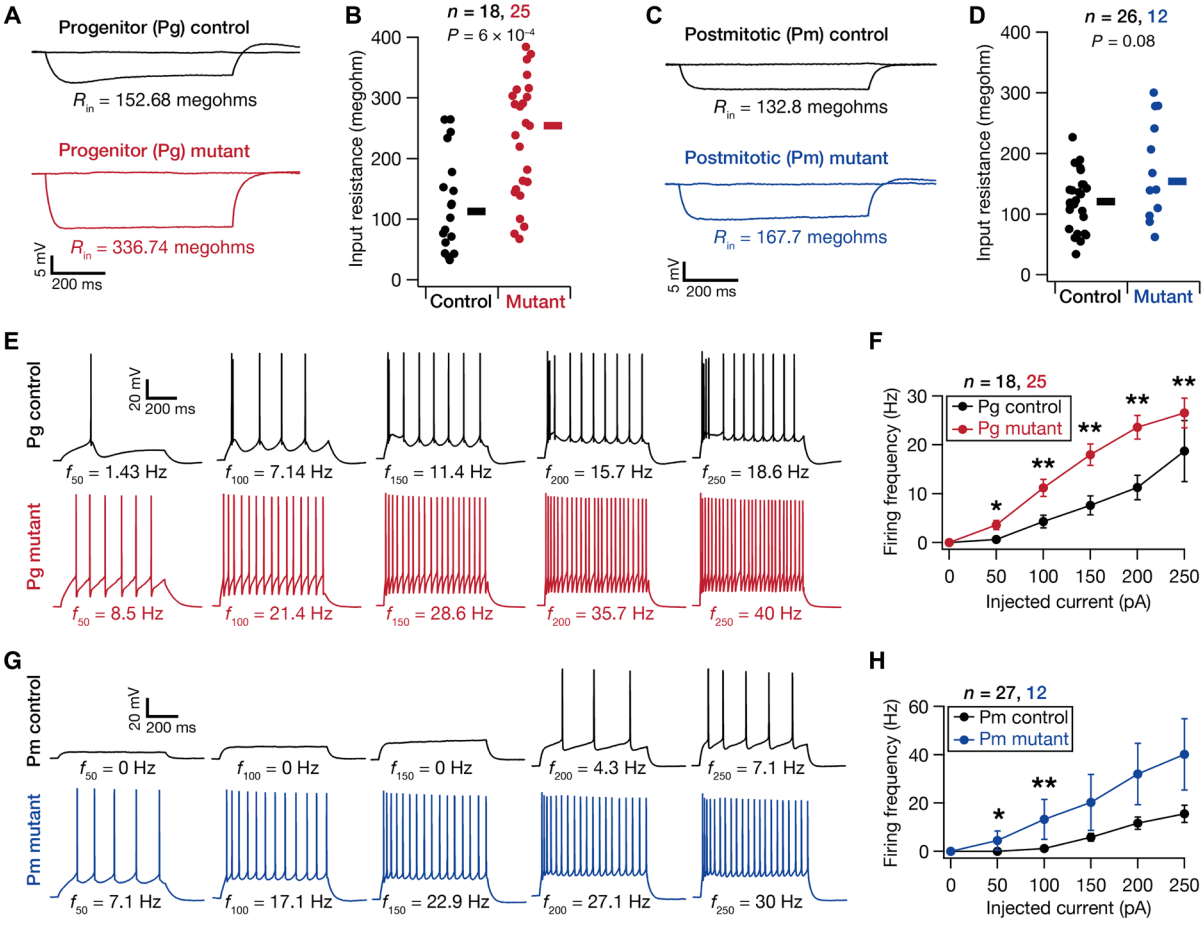

Fig. 2. Loss of *Lhx2* either in Pg or newborn Pm neurons enhanced intrinsic excitability of neocortical layer II/III pyramidal neurons. (**A**) Example voltage responses of neurons to pulse current injections of −50 pA and 0 pA, used for computing input resistance (R_{in}). (**B**) Beeswarm plots of input resistance (R_{in}) obtained from control and Pg mutant neurons. The thick line on the right of each beeswarm plot depicts the respective median values. (**C** and **D**) Same as (A) and (B), for Pm mutant neurons and associated controls. (**E**) Voltage traces recorded from example pyramidal neurons in response to 50 to 250 pA pulse current injections from control (top panels) and Pg mutant (bottom panels) mice. The firing rate associated with each trace is provided at the bottom of the trace. (**F**) Mean-SEM plot showing firing rates of neurons from control and Pg mutant mice plotted against current injection amplitudes. (**G** and **H**) Same as (E) to (F), for Pm mutant neurons and associated controls. Statistical test: Wilcoxon rank sum test: $*P < 0.05$ and $**P < 0.01$. *n* represents the number of total neurons recorded in each group. Additional analyses of sub- and suprathreshold measurements from all four groups are provided in figs. S3 to S7.

cell fate commitment in the progenitors. Therefore, we sought to examine whether the subtype identity of the Pg mutant neurons was disrupted. We found multiple aspects of the upper layer identity to be preserved in the mutants. These neurons migrated to the correct layer, expressed the upper layer marker POU3F2 similar to controls (Fig. 3, A and B), and displayed a characteristic pyramidal morphology (Fig. 3C). We also examined whether Pg *Lhx2* mutant neurons extended projections via the corpus callosum. Previous studies reported that loss of *Lhx2*, driven by *Emx1*-Cre or *Nestin*-Cre, which act in cortical progenitors from E11.5, resulted in corpus callosum agenesis, whereas inactivation using *Nex*-Cre did not (*21*).

We used IUE to investigate the impact of cell-autonomous, progenitor-specific deletion of *Lhx2* on callosal subtype identity of layer II/III neurons by electroporating Cre-TdTomato in the progenitors of $Lhx2^{lox/lox}$; Ai9 (mutant) and Ai9 (Control) mice at E15.5. The corpus callosum was examined at P7 and P30.

In contrast to the notable effects on dendritic morphology, the axons of Pg mutant neurons did not appear to be significantly affected. The corpus callosum traversed the midline (Fig. 3, D and E), reached the contralateral hemisphere, and developed arbors at layer V and layer II/III by P30 (Fig. 3F). These data conclusively demonstrate that the corpus callosum agenesis reported using *Emx1*-Cre or *Nestin*-Cre (*21*) is not due to a cell-autonomous role for LHX2 in the neurons of layer II/III. The normal callosal projections of Pg mutant neurons also confirm that their callosal subtype identity is not grossly derailed.

To gain mechanistic insights into these phenotypes, we performed transcriptomic analysis to profile the genes dysregulated in Pg and Pm mutant layer II/III neurons compared with their respective controls. We isolated E15.5-electroporated Pg and Pm mutant neurons, together with littermate controls, at P5 and performed RNA sequencing (RNA-seq) analysis (Fig. 3, G and I). We examined these datasets for well-established markers of neuronal subtype identity, including deep layer markers like *Tbr1*, *Fezf2*, *Tle4*, *Sox5*, *Bcl11a*, *Bcl11b*, and upper layer markers like *Cux1*, *Cux2*, *Pou3f1*, *Rorb*. We found no gross dysregulation of these genes in either Pg or Pm mutant neurons at P5, suggesting

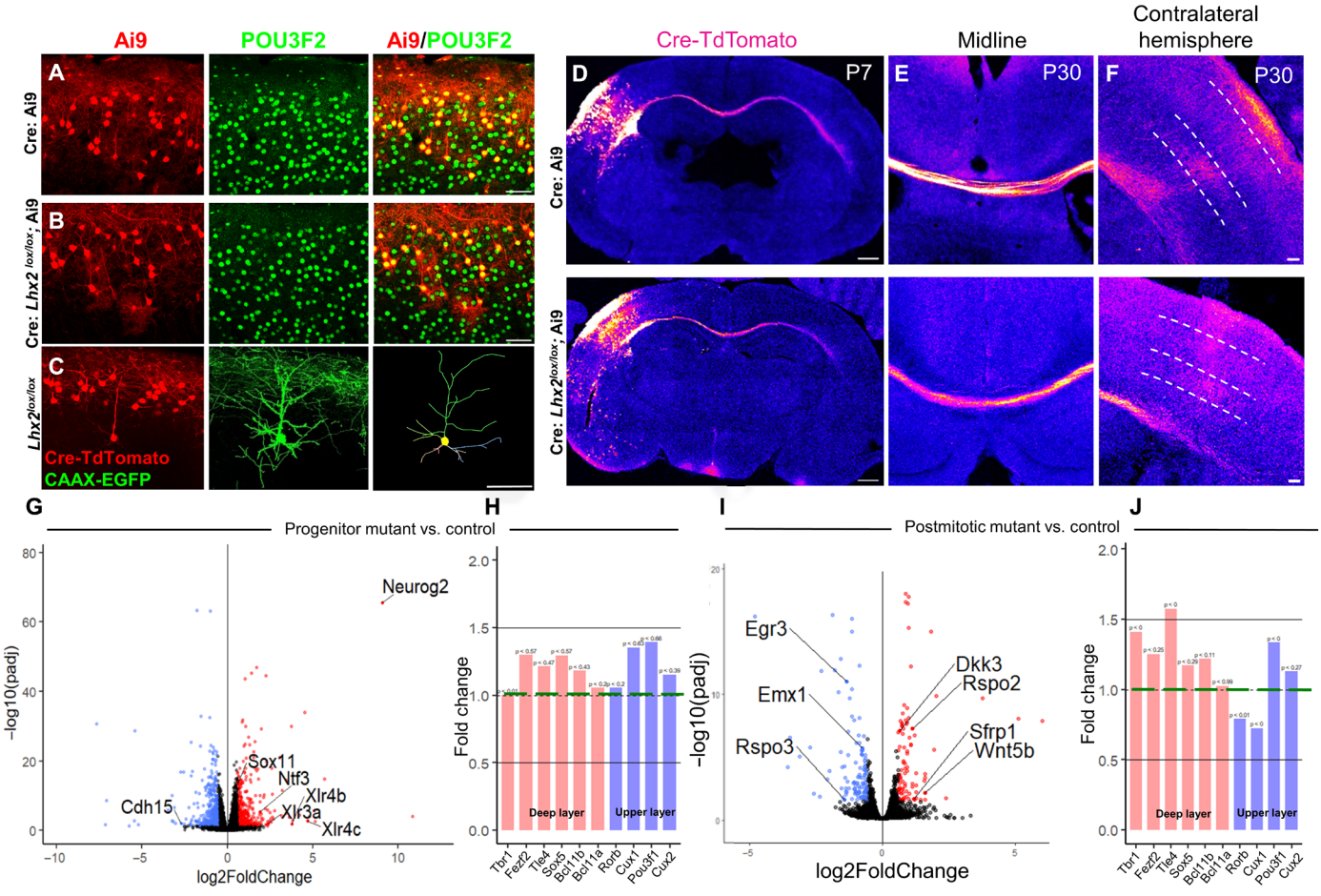

Fig. 3. Loss of *Lhx2* does not affect the differentiation of the neurons. (**A** to **C**) Loss of *Lhx2* does not affect the expression of the upper-layer marker POU3F2. Cre electroporation in Ai9 embryos at E15.5 labels POU3F2-positive upper-layer neurons (A). Cre electroporation in *Lhx2*$^{lox/lox}$; Ai9 progenitors does not alter POU3F2 expression (B). (C) Cre-TdTomato electroporation enables cell-autonomous deletion of *Lhx2*, and co-electroporation of CAAX-EGFP allows dendritic arbor visualization. Arbors were 3D reconstructed using Neurolucida software. Analyses were performed at P30. Scale bars, 50 μm. (**D** to **F**) Axons of control and *Lhx2* progenitor (Pg) mutant neurons project through the corpus callosum at P7 (D) and arborize in the contralateral hemisphere by P30 (E and F). (**G** and **I**) Volcano plots showing differentially expressed genes from RNA-seq of E15.5-labeled control and *Lhx2* mutant neurons collected at P5 (Pg mutants in G, Pm mutants in I). (**H** and **J**) Fold-change analysis of deep-layer (red) and upper-layer (blue) marker genes in control versus *Lhx2* mutant neurons (Pg mutants in H, Pm mutants in J).

that their molecular subtype identity is broadly preserved (Fig. 3, H and J, and tables S2 and S3).

In summary, although LHX2 is a pleiotropic factor, its function in the maturation of layer II/III neurons appears to be confined to their dendritic processes and spines, not their axons or any other aspect of their molecular subtype identity that we examined. In the following sections, we examined the molecular mechanisms dysregulated in neurons arising from Pg and Pm loss of *Lhx2*.

The Pg mutant dendritic arborization phenotype is recapitulated upon loss of *Lhx2* exclusively from basal progenitors

The transcriptomic analysis of genes dysregulated in Pg mutant neurons revealed that the expression of transcription factor *Neurog2* was 535-fold up-regulated over control neurons at P5 (Fig. 3G and table S2). NEUROG2, known for its transient expression during the early stages of neuronal differentiation, has been previously implicated in regulating neuronal polarity and dendritogenesis in cortical neurons (*13*). We explored the potential genetic interaction between *Lhx2* and *Neurog2* in regulating layer II/III morphometry.

Analysis of the single-cell RNA-seq (scRNA-seq) dataset of E15.5 neocortical cells obtained from Di Bella *et al.* (*28*) revealed that while *Lhx2* is enriched in both apical and basal progenitors during neurogenesis, *Neurog2* is selectively enriched in the *Eomes*-positive basal progenitors and is absent in postmitotic neurons [Fig. 4, A to D; (*29*)]. Therefore, we investigated whether the relevance of the progenitor-specific role of *Lhx2* in regulating neuronal dendritogenesis is restricted to the basal progenitors using an *Eomes*-driven Cre recombinase (*30*) (Fig. 4, E to E”).

Sholl analysis of apical and basal dendrites of *Eomes*-Cre–driven *Lhx2* mutant neurons demonstrated a near-perfect overlap of the two progenitor mutant graphs (Cre- and *Eomes*-Cre), indicating that the role of LHX2 in regulating dendrite morphometry at postmitotic stages is relevant in basal, not apical progenitors, that go on to produce layer II/III neurons (Fig. 4, F and G). Dendritic spine analysis of *Eomes*-Cre–driven *Lhx2* mutant neurons also showed recapitulation of the Pg mutant phenotype (fig. S9).

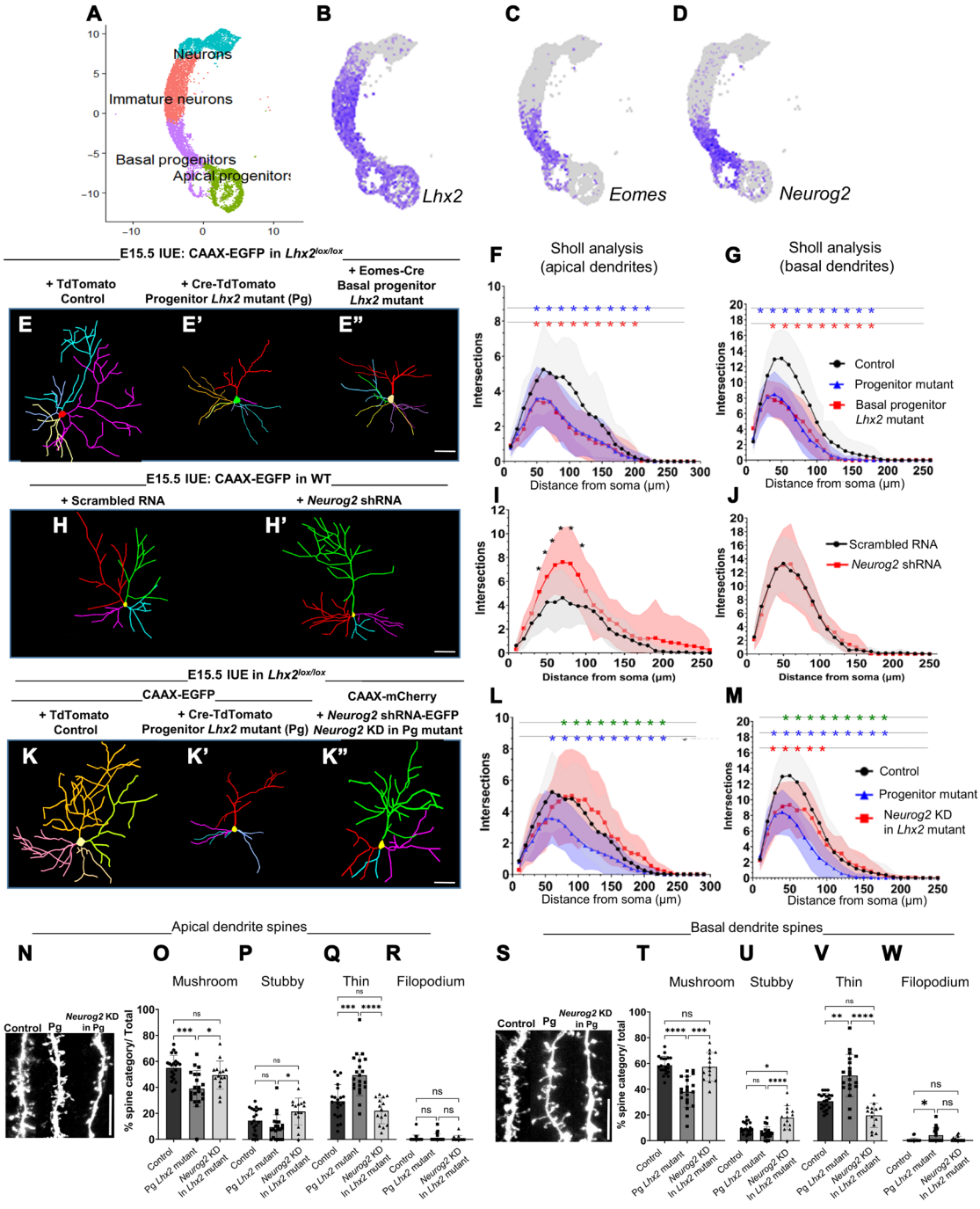

Fig. 4. LHX2 modulates dendritic morphogenesis of neurons by suppression of *Neurog2* in progenitors. (**A** to **D**) scRNA-seq analysis at E15.5 (*28*) shows that *Lhx2* is expressed in apical progenitors, basal progenitors, and immature neurons (B), while *Neurog2* expression (D) is restricted to *Eomes*-positive basal progenitors (C). (**E** to **G**) Dendritic morphology comparisons among Control, pan-progenitor (Pg) mutant, and basal progenitor-specific *Lhx2* mutant neurons show that loss of *Lhx2* in basal progenitors (E to E″) phenocopies the dendritic morphology of Pg mutants in both apical (F) and basal (G) compartments. (**H** to **J**) Neurolucida tracings (H and H′) and Sholl analysis of apical (I) and basal (J) dendrites reveal that *Neurog2* knockdown increases dendritic complexity specifically in apical dendrites. (**K** to **M**) Rescue experiments using *Neurog2* shRNA in Pg mutants (K to K″) demonstrate complete restoration of apical dendritic complexity (L) and partial rescue of basal dendrites (M). In each group, 30 to 35 neurons were analyzed from three independent experiments. Statistics: Two-way ANOVA with Tukey's multiple comparisons correction; asterisks in (I) and (J) indicate pairwise comparisons: Control versus basal progenitor mutant (red), control versus Pg mutant (blue), and Pg mutant versus basal progenitor mutant (green); asterisks in (L) and (M) indicate: Control versus Neurog2 KD in Pg mutant (red), control versus Pg mutant (blue), and Pg mutant versus Neurog2 KD in Pg mutant (green). Detailed *P* values for each intersection are provided in fig. S8 and data S1. (**N** to **W**) Spine morphology analysis of apical and basal dendrites across control, Pg mutant, and Neurog2 KD in Pg mutant neurons shows significant rescue of spine morphology defects. Significance levels: $*P < 0.05$, $**P < 0.01$, $***P < 0.001$, and $****P < 0.0001$. Scale bars: 50 μm (E to E″, H to H′, and K to K″) and 5 μm (N and S).

Knockdown of *Neurog2* partially rescues the *Lhx2* progenitor mutant dendritic defect

To test whether LHX2 acts via *Neurog2* to regulate dendritic morphology, we used a short-hairpin RNA construct, previously used to knock down *Neurog2* (*31*) (fig. S10). First, we analyzed the effect of shRNA-mediated knockdown of *Neurog2* alone in E15.5 progenitors, compared with scrambled shRNA as control (Fig. 4, E and E'). At P28, neurons arising from these progenitors showed a significantly higher dendritic complexity of apical dendrites of Layer II/III neuron apical dendrites but no change in basal dendrites (Fig. 4, I and J), correlating with the previously known role of *Neurog2* (*13*). Next, we investigated whether the simultaneous *Neurog2* knockdown and *Lhx2* knockout in progenitors could rescue the dendritic and spine morphology defects. We electroporated E15.5 $Lhx2^{lox/lox}$ progenitors with the *Neurog2* shRNA construct together with Cre and CAAX-mCherry (Fig. 4, K to K").

Sholl analysis of these neurons at P30 demonstrated a significant and complete rescue of the dendritic defect phenotype in the apical dendrites and a significant partial rescue in the basal dendrites compared with a loss of *Lhx2* alone (Fig. 4, L and M, and fig. S8). Spine morphology analysis in the apical and basal dendrites of these neurons also revealed substantial amelioration of the spine defects compared with a loss of Lhx2 alone (Fig. 4, N to W).

In summary, these results indicate that LHX2 plays a crucial role in E15.5 basal progenitors, which results in suppression of *Neurog2* expression in their subsequent postmitotic neuronal progeny. This suppression is required for the normal development of dendritic arbors and spine morphogenesis in layer II/III cortical neurons.

Constitutive activation of β-Catenin recapitulates the dendritic morphology phenotype of loss of *Lhx2*

A comparative transcriptomic analysis of Pg and Pm *Lhx2* mutant neurons (Fig. 3, G and I) revealed 11 commonly up-regulated and 15 commonly down-regulated genes. *Neurog2* expression remained unchanged when *Lhx2* was deleted specifically from postmitotic neurons (Fig. 3I), suggesting that LHX2-mediated regulation of *Neurog2* likely occurs at the progenitor stage, before neurons become postmitotic. A failure in this regulatory mechanism results in an aberrant up-regulation of *Neurog2* in the neurons derived from the mutant progenitors, by P5.

To investigate the mechanisms underlying the dendritic defects specifically caused by the postmitotic loss of *Lhx2*, we further examined the commonly dysregulated genes to identify shared pathways disrupted in both progenitor- and postmitotic-specific *Lhx2* mutants. Several of these genes were associated with the Wnt signaling cascade, including *Wnt5b*, *Rspo2*, *Sfrp1*, and *Rspo3* (Fig. 5A and table S3). Consistently, gene ontology analysis of the Pm *Lhx2* transcriptome identified "regulation of the canonical Wnt signaling pathway" as one of the top dysregulated categories (Fig. 5B). This prompted us to investigate whether canonical Wnt signaling is disrupted following the postmitotic loss of *Lhx2*. A typical readout of active canonical Wnt signaling is the stabilization of cytoplasmic β-Catenin and its translocation to the nucleus (*32*). Immunostaining for β-CATENIN in layer II/III Pm mutant neurons revealed a significant increase in nuclear localization (Fig. 5, C and D).

We tested whether directly stabilizing β-catenin can recapitulate the dendritic defects observed upon loss of *Lhx2* using a *Ctnnb1* (β-CATENIN) conditional gain-of-function (GOF) mouse line. Cre-mediated recombination of exon 3 prevents β-CATENIN from being phosphorylated and tagged for degradation, thus resulting in a constitutively stabilized β-CATENIN protein (*33*). Since the perturbation of β-CATENIN is extremely disruptive in progenitors (*34*), we examined this using a postmitotic neuron–specific, Doublecortin (*Dcx*) promoter–driven Cre recombinase (*Dcx*-Cre). A plasmid encoding *Dcx*-Cre was electroporated at E15.5 together with CAAX-EGFP for labeling purposes (Fig. 5, E to E"). Neurons arising from electroporated progenitors would be expected to display β-catenin GOF upon becoming postmitotic and were scored at P30.

Sholl analysis of the apical dendrites of the *Ctnnb1* GOF neurons showed a striking recapitulation of the apical and basal dendritic defects seen in the Pm *Lhx2* mutant condition (Fig. 5, F and G, and fig. S8). *Ctnnb1* GOF neurons also recapitulated the spine defects observed in postmitotic *Lhx2* mutant neurons, i.e., an increase in the proportion of thin morphology spines and a concomitant decrease in mushroom morphology spines in both apical and basal dendrites (Fig. 5, H to Q).

In summary, these demonstrate that constitutive activation of β-Catenin partially phenocopies the dendritic and spine morphology defects observed upon postmitotic loss of *Lhx2*, implicating dysregulated Wnt signaling as a key downstream effector in this process.

DISCUSSION

Our results demonstrate that *Lhx2* disruption in progenitors or newborn postmitotic neurons has lasting effects on gene regulation, dendritic arborization, and electrophysiological properties of postmitotic neurons. While some phenotypes overlap in Pg and Pm mutant neurons, key differences highlight stage-dependent functions of this transcription factor.

One striking consequence of *Lhx2* loss in progenitors is the aberrant up-regulation of *Neurog2* in postmitotic neurons. *Neurog2* plays a crucial role in neuronal differentiation, migration, and maturation (*13*, *35*–*37*). Previous studies have shown that NEUROG2 is necessary for establishing the unipolar leading process in migrating cortical neurons (*13*). Our findings expand these functions to include the modulation of dendritic morphometry and spine maturation. Using the Cre electroporation strategy, we induce long-term *Lhx2* loss, affecting both progenitors and their postmitotic neuronal progeny, which leads to significant up-regulation of *Neurog2*. While this paradigm does not specify the exact stage at which *Neurog2* up-regulation produces functional consequences, its normal restriction to early developmental stages, particularly basal progenitors, suggests that its dysregulation in postmitotic neurons may drive dendritic defects. Under normal conditions, *Neurog2* expression peaks in basal progenitors and then declines once neurons become postmitotic. However, when *Lhx2* is lost in progenitors, this down-regulation of *Neurog2* is notably impaired, resulting in its persistent expression in postmitotic neurons. *Neurog2* is not up-regulated when *Lhx2* is disrupted solely in postmitotic neurons, indicating a unique role of *Lhx2* in progenitors that ensures the suppression of *Neurog2* at later stages. Therefore, we have identified a unique function of LHX2 in progenitors that is essential for the postmitotic suppression of *Neurog2*.

The loss of *Lhx2* and down-regulation of *Neurog2* individually exert opposite effects on apical dendritic complexity, with *Lhx2* loss reducing complexity while *Neurog2* down-regulation enhances it. However, when both manipulations are applied together, apical dendritic complexity is fully restored, suggesting that although *Neurog2*

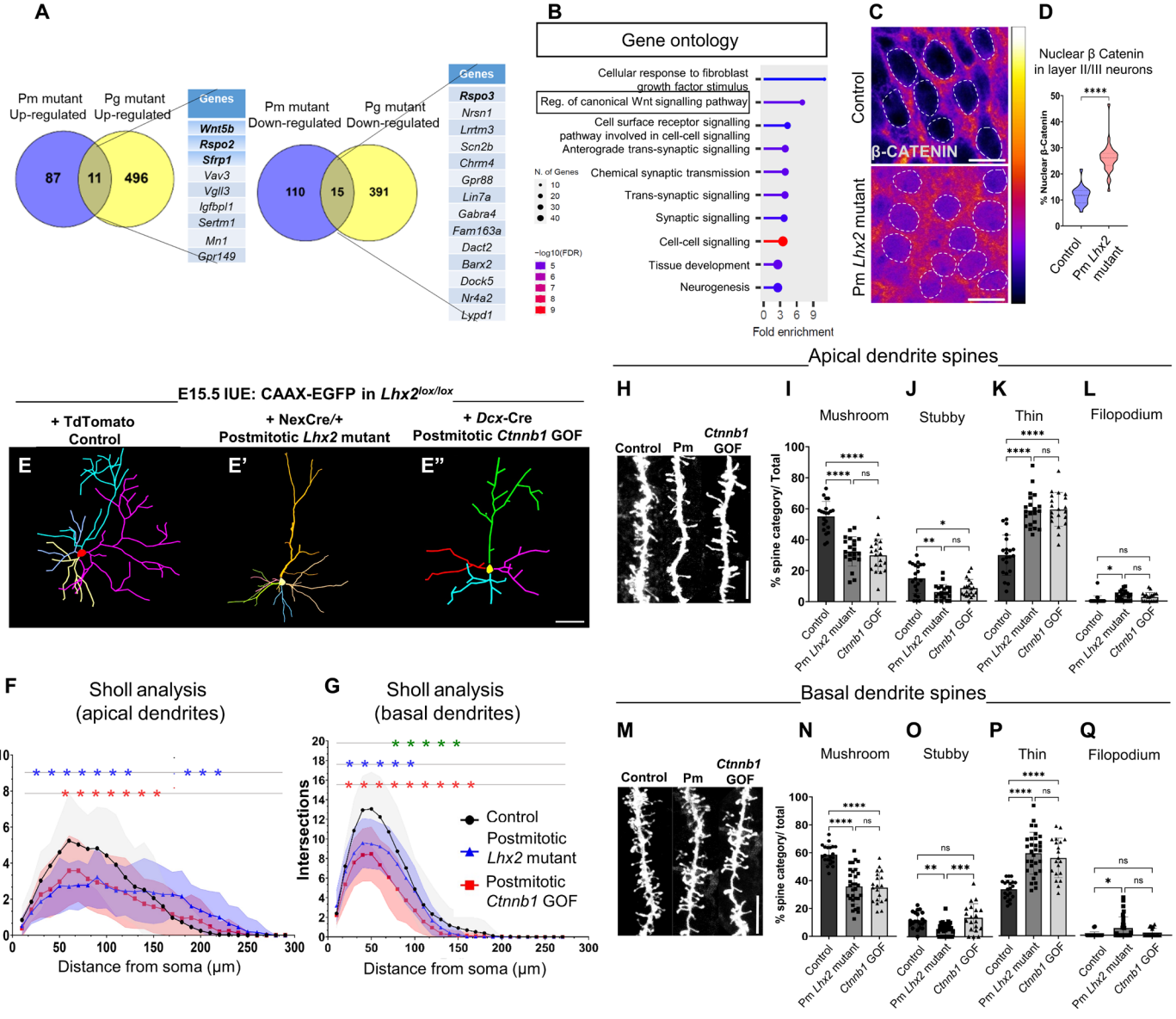

Fig. 5. *Lhx2* regulates canonical Wnt signaling in postmitotic neurons. (**A** and **B**) Comparative analysis of Pg and Pm *Lhx2* mutant RNA-seq datasets reveals up-regulated (A) and down-regulated (B) genes, including Wnt signaling pathway genes, as confirmed by gene ontology (GO) analysis (B). (**C** and **D**) Layer II/III Pm *Lhx2* mutant neurons display increased nuclear localization of the Wnt signaling downstream effector, β-CATENIN. (**E** to **E″**) Neurolucida tracings of control, Pm *Lhx2* mutant, and *Dcx*-Cre–driven *Ctnnb1* GOF neurons at P30. (**F** and **G**) Sholl analysis of apical and basal dendrites shows similar dendritic defects in Pm *Lhx2* mutant and *Ctnnb1* GOF neurons. Thirty to 40 neurons in each category were analyzed from four biologically independent experiments. Statistical test: Two-way ANOVA multiple comparisons with Tukey's correction; asterisks indicate pairwise comparisons between control versus Ctnnb1 GOF (red), control versus Pm mutant (blue), and Pm mutant versus Ctnnb1 GOF (green) detailed statistical significance values per intersection row provided in fig. S8 and data S1. (**H** to **Q**) Dendritic spine morphology defects are comparable between Pm *Lhx2* mutant and *Ctnnb1* GOF neurons. Both apical and basal dendrites exhibit a significant reduction in mushroom and stubby morphology spines (I, J, N, and O) and a concomitant increase in thin and filopodium morphology spines (K, L, P, and Q; 0.20 dendrites with 25 spines each were analyzed for each category. Statistical test: Kruskal-Wallis Test for spine morphology analysis). For (F), (G), and (H) to (Q), $*P < 0.05$, $**P < 0.01$, $***P < 0.001$, and $****P < 0.0001$. Scale bars are 50 μm in (E) to (E″), 10 μm in (C), and 5 μm in (H) and (M).

is a downstream target of *Lhx2*, each factor may independently regulate common or distinct pathways controlling dendritic architecture. In contrast, for basal dendrites, down-regulation of *Neurog2* alone has no effect, and the loss of *Lhx2* alone reduces complexity. When both manipulations are combined, there is a partial rescue of basal dendritic complexity, indicating that *Lhx2* influences dendritic morphology through multiple pathways, some of which cannot be compensated for by *Neurog2* down-regulation alone. Since NEUROG2 is a pleiotropic transcriptional regulator (*38*) implicated in pioneering chromatin interactions essential for differentiation (*35*), and LHX2 regulates its expression during upper-layer neurogenesis, understanding how these factors function epigenetically in tandem to regulate specific developmental programs will be a fruitful avenue for future investigation.

An intriguing finding in our study is that *Neurog2* remains unchanged in Pm *Lhx2* mutant neurons, suggesting that LHX2 occupancy of the open chromatin of postmitotic neurons differs significantly from that in progenitors. We hypothesize that *Lhx2* loss in progenitors may induce epigenetic changes that prevent loci such as *Neurog2* from epigenetic repression, leading to an aberrant overexpression. *Lhx2* has been shown to interact with the NuRD chromatin remodeling complex (*39*), supporting a possible role in epigenetic regulation that warrants further investigation.

These findings also provide novel insights into how LHX2 functions evolve across various stages of neurogenesis. Previous studies identified an early cortical progenitor-specific role of LHX2 that regulates the electrophysiological properties of the firstborn cells of the cortex, known as the subplate (*18*). At mid-developmental stages, *Lhx2* governs deep-layer neuronal fate by regulating *Fezf2* expression and layer V identity (*39*). Here, we demonstrate yet another later-stage role of *Lhx2* in regulating dendritic morphogenesis in superficial layer II/III neurons. In this case, we do not find evidence of altered neuronal subtype markers, and the overall pyramidal structure, positioning, and axonal connectivity of these layer II/III neurons remain intact. Therefore, the overall deficit appears limited to a specific feature of these neurons: their dendritic arbor morphogenesis. Together, these studies indicate that LHX2 plays distinct roles as progenitors mature and in postmitotic neurons. Consequently, it is expected that the transcriptomic dysregulation datasets observed in Pg and Pm mutant neurons have limited overlap. The broadly similar phenotypes seen in Pg and Pm mutant dendritic arbors are distinct and may result from different pathways or partly from common pathways such as the Wnt signaling pathway.

Our findings also suggest that the constitutive activation of β-catenin signaling mimics the dendritic arborization phenotype of Pg and Pm *Lhx2* mutant neurons. The dysregulation of Wnt pathway members in both transcriptomic datasets suggests an interaction between LHX2 and this pathway to regulate dendritic morphogenesis. Suppressing canonical Wnt signaling in postmitotic layer II/III neurons while simultaneously knocking out *Lhx2* would provide definitive evidence of this interaction, representing an important direction for future exploration. While the role of Wnt signaling in neuron polarity and dendritogenesis is well established (*38*, *40*), our study adds another layer of complexity. We show that enhanced Wnt signaling in postmitotic layer II/III neurons of the lateral somatosensory cortex reduces dendritic complexity, contrary to its reported function in the medial cortex (*41*, *42*). These findings suggest that the molecular context of each neuronal subtype influences how Wnt signaling shapes dendritic architecture. In addition, since *Lhx2* is expressed in superficial layer neurons into adulthood, its potential role in maintaining dendritic structures via the Wnt pathway remains an open question. Understanding these spatial differences in signaling pathway responsiveness will be critical for future research. Together, these findings provide valuable insights into the spatial differences in the functionality and responsiveness of signaling cascades and their transcriptional regulation.

In addition to morphological features, we also report that *Lhx2* loss profoundly alters the electrophysiological properties of layer II/III neurons, leading to a pronounced increase in intrinsic excitability. This observation raises exciting new questions about how *Lhx2* regulates ion channel expression or synaptic function, which will be important avenues for future studies.

Our findings provide fundamental insights into how *Lhx2* governs neuronal maturation, function, and circuit development. Given that LHX2 haploinsufficiency in humans is linked to autism spectrum disorder, intellectual disability, and microcephaly (*43*), understanding its cell type–specific regulatory networks is a crucial step toward uncovering the molecular mechanisms underlying these disorders.

MATERIALS AND METHODS

Mice

All procedures followed the Tata Institute of Fundamental Research Animal Ethics Committee (TIFR-IAEC) guidelines. The *Lhx2*$^{lox/lox}$ mouse line was a gift from E. Monuki (University of California, Irvine, USA). The *Ai9* reporter mouse line (strain no. 007909) was obtained from Jackson Laboratory. The *NexCre*/+ mouse line was received from Klaus Nave, Max Planck Institute for Experimental Medicine (*20*). The *Ctnnb1* conditional GOF mouse line was obtained from M. M. Taketo (Kyoto University, Japan). All animals were kept at an ambient temperature and humidity, with a 12-hour light-dark cycle and food available ad libitum. Noon of the day of the vaginal plug was designated as E0.5. Both male and female animals were used for all experiments.

All the electrophysiology recording experiments were reviewed and approved by the Institute Animal Ethics Committee of the Indian Institute of Science, Bangalore. Experimental procedures were similar to previously established protocols (*44*–*46*) and are detailed below. Seven (four males and three females) mice from the Pm control group between 7 and 9 months old, seven (three males and four females) from Pm *Lhx2* mutant mice between 6 and 10 months old, four (two males and two females) mice belonging to the Pg control group between 2 and 4 months old, and five (three males and two females) Pg *Lhx2* mutant mice between 2 and 4 months old were used for in vitro patch-clamp electrophysiology experiments. Animals were provided ad libitum food and water and were housed with an automated 12-hour light-dark cycle, with the facility temperature maintained at 23°C.

Primers for genotyping were as follows (expected band sizes): *Lhx2* conditional forward, ACCGGTGGAGGAAGACTTTT; *Lhx2* conditional reverse, CAGCGGTTAAGTATTGGGACA (WT, 144 bp; *Lhx2*^{lox}, 188 bp; and null: 231 bp); *NexCre* forward, GAGTCCTGGAATCAGTCTTTTTC; *NexCre* reverse, AGAATGTGGAGTAGGGTGAC; and *NexCre* mutant reverse, CCGCATAACCAGTGAAACAG (WT, 770 bp; and *NexCre*, 525 bp).

IUE and DNA constructs

IUE was performed at E15.5, as previously described (*18*). Embryos were injected with plasmid DNA solution dissolved in nuclease-free water with 0.1% fast green with plasmid DNA into the lateral ventricle through the uterine wall using a fine glass microcapillary (Sutter capillaries no. B100-75-10).

The pCAGGS-IRES-TdTomato construct was obtained from Addgene (no. 83029). pCAGGS-IRES-Cre-TdTomato was generated in the lab. Membrane-bound EGFP (CAAX-EGFP) and mCherry (CAAX-mCherry) were gifts from M. Sonawane (Tata Institute of Fundamental Research, India). *Eomes*-Cre was obtained from T. Haydar (University of Maryland, Baltimore, USA). *Dcx*-Cre was previously described in (*47*). Silcaggs-*Neurog2* shRNA-EGFP and Silcaggs-scrambled-EGFP were gifts from François Guillemot (Francis Crick Institute, London, UK).

Tissue preparation

Electroporated mice were harvested on P30. Mice were anesthetized using thiopentone and transcardially perfused with Saline, followed by 4% (w/v) paraformaldehyde in phosphate buffer. Brains were kept for overnight fixation and then cryoprotected by transferring to 30% sucrose–phosphate-buffered saline until sectioning. The brains were sectioned at 40 μm using a Vibratome (Leica VT2000S).

Immunohistochemistry

Brains were sectioned at 40 μm and processed for free-floating immunohistochemistry. Sections were washed and permeabilized with phosphate buffer containing 0.3% (v/v) Triton X-100. Blocking was done with 5% (v/v) horse serum in phosphate buffer with 0.3% (v/v) Triton X-100 for 1 hour at room temperature. Primary antibody treatment was performed in phosphate buffer containing 0.3% (v/v) Triton X-100 with 2.5% (v/v) horse serum and incubated overnight at 4°C. The sections were washed in phosphate buffer, followed by the appropriate secondary antibody for 2 hours at room temperature and 4′,6-diamidino-2-phenylindole. Sections were mounted on Superfrost plus glass microscope slides (catalog no. 71869-10) and protected with Fluoroshield (Sigma-Aldrich catalog no. F6057 or F6182). Antibodies used were as follows: biotinylated GFP (Abcam; ab6658, 1:200), rabbit red fluorescent protein (Abcam; ab65856, 1:200), Neurog2 (Thermo Fisher Scientific; PA5-78556, 1:1000), and β-Catenin (BD Biosciences; A610151, 1:200).

Image acquisition and analysis

Images of neurons and dendritic spines were imaged using Olympus FluoView 1200 and 3000 confocal microscopes with FluoView software. A step size of 0.8 μm was kept to maximize the *z*-axis resolution of the dendritic branches. All the image analysis was done on Fiji ImageJ. A nonlinear operation such as gamma correction was not performed in the images. Brightness and contrast adjustments were performed identically for control and mutant conditions.

Dendritic morphology and spine analysis

3D morphology reconstruction of CAAX-EGFP/CAAX-mCherry–labeled neurons was done using the Neurolucida 2017 software. The apical and basal dendrites were identified on the basis of the directionality of the dendrites. The primary dendrite directed toward the pial surface of the cortex was considered apical, and the rest were labeled as basal. Total length, mean length, and Sholl analysis were performed using the Neurolucida Explorer 2017 software.

For dendritic spine analysis, high-resolution images of the distal branches of the apical and basal dendrites were acquired on the confocal system. The ImageJ plugin Dendritic Spine Counter (https://imagej.net/plugins/dendritic-spine-counter) was used to classify spines into mushroom, stubby, thin, or filopodium by calculating the neck length, neck width, and head width of the spines. Approximately 15 to 20 dendrites with ~25 spines each, obtained from four biological replicates, were analyzed. Kruskal Wallis Test was performed to compare the three conditions. All statistical analysis was performed using GraphPad Prism 10.0.0 software. Error bars in graphs excluding electrophysiology experiments indicate Standard Deviation.

RNA-seq and analysis

For RNA-seq, the E15.5 electroporated layer II/III (control, EGFP in $Lhx2^{lox/lox}$; progenitor mutant, Cre-EGFP in $Lhx2^{lox/lox}$; postmitotic mutant EGFP in *NexCre/+* $Lhx2^{lox/lox}$) was microdissected from the cortical tissue at P5 after sectioning on a tissue chopper. RNA extraction and sequencing were performed on four replicates of each condition. One microgram of RNA was used for cDNA library preparation. Samples were sequenced using the Illumina HiSeqX platform to achieve 2 × 150 bp reads to generate 60 million paired-end reads per sample.

FastqQC was performed as described in (FastQC), and read with Phred scores higher than 30 were aligned using HISAT2 (*48*). Feature counts function of the R Subread package was used to quantify the number of reads per transcript. Differential expression analysis was performed using DESeq2 (*49*). A log2FoldChange cutoff of 0.58 and P value <0.05 was used to identify differentially expressed genes. Gene ontology analysis was performed using ShinyGO online software (*50*).

In vitro primary neuronal cultures

Neuronal cultures were performed from E15.5 embryos of $Lhx2^{lox/lox}$ and *NexCre/+;* $Lhx2^{lox/lox}$ mice. Embryos were dissected in ice-cold L-15 medium (Thermo Fisher Scientific SKU no. 41300039). pCAGGS-IRES-Cre-TdTomato + CAAX-EGFP (progenitor mutant) and pCAGGS-IRES-TdTomato + CAAX-EGFP (control) were electroporated in the dissected brains of $Lhx2^{lox/lox}$ mice. For the postmitotic loss condition, CAAX-EGFP was electroporated in *NexCre/+*, $Lhx2^{lox/lox}$ (postmitotic mutant), and littermate $Lhx2^{lox/lox}$ controls. The electroporated cortical explants were maintained on a Millicell Insert (Millipore, catalog no. 217 PICM03050) with neurobasal medium (Thermo Fisher Scientific SKU no. 21103049) containing B-27 supplement (Thermo Fisher Scientific SKU no. 17504044) and 1% GlutaMAX (Thermo Fisher Scientific SKU no. 35050061) for 4 hours at 37°C with 5% CO_2. The explants were dissociated into a single-cell suspension using 0.25% trypsin (Thermo Fisher Scientific SKU no. 15400054) and then dissociated by trituration after washes. The dissociated cells were plated on poly-D-lysine–coated (Sigma-Aldrich catalog no. P7280) coverslips in neurobasal medium containing B-27 supplement, penicillin/streptomycin, and 1% GlutaMAX for 15 days at a 5% CO_2 atmosphere.

Dendritic morphology was analyzed using the NeuronJ plugin in ImageJ. Apical and basal dendrites were identified on the basis their pyramidal morphology. Only neurons with just one apical dendrite were considered for analysis.

In vitro patch-clamp electrophysiology

Slice preparation for in vitro patch-clamp recording

Mice were anesthetized by intraperitoneal injection of a ketamine-xylazine mixture. After the onset of deep anesthesia, assessed by cessation of the toe-pinch reflex, transcardial perfusion of the ice-cold cutting solution was performed. The cutting solution contained 2.5 mM KCl, 1.25 mM NaH_2PO_4, 25 mM $NaHCO_3$, 0.5 mM $CaCl_2$, 7 mM $MgCl_2$, 7 mM dextrose, 3 mM sodium pyruvate, and 200 mM sucrose (pH 7.3, ~300 mOsm) saturated with carbogen (95% O_2 and 5% CO_2). Thereafter, the brain was removed quickly, and 350-μm-thick near-horizontal slices were prepared with a vibrating blade microtome (Leica Vibratome) while submerged in an ice-cold cutting solution saturated with carbogen. The slices were then incubated for 10 to 15 min at 34°C in a holding chamber containing a holding solution (pH 7.3, ~300 mOsm) with the composition of 125 mM NaCl, 2.5 mM KCl, 1.25 mM NaH_2PO_4, 25 mM $NaHCO_3$, 2 mM $CaCl_2$, 2 mM $MgCl_2$, 10 mM dextrose, and 3 mM sodium pyruvate saturated with carbogen. Thereafter, the slices

were kept in the holding chamber at room temperature for at least 30 min before recordings started.

Whole-cell current-clamp recordings

For electrophysiological recordings, slices were transferred to the recording chamber and were continuously perfused with carbogenated artificial cerebrospinal fluid (ACSF; extracellular recording solution) at a flow rate of 2 to 3 ml/min. All neuronal recordings were performed under current-clamp configuration at physiological temperatures (32° to 35°C) achieved through an inline heater that was part of a closed-loop temperature control system (Harvard Apparatus). The ACSF contained 125 mM NaCl, 3 mM KCl, 1.25 mM NaH_2PO_4, 25 mM $NaHCO_3$, 2 mM $CaCl_2$, 1 mM $MgCl_2$, and 10 mM dextrose (pH 7.3; ~300 mOsm). Slices were first visualized under a 10× objective lens to visually locate layer II/III of the somatosensory cortex (S1). A 63× water-immersion objective lens was used to perform visually guided patch-clamp recordings from mCherry-labeled pyramidal neurons (Pm control and Pm *Lhx2* neurons; unlabeled for Pg control and Pg *Lhx2* neurons) in superficial layers of S1 through a Dodt contrast microscope (Carl Zeiss Axioexaminer). Whole-cell current-clamp recordings were performed from layer II/III S1 pyramidal neurons with a Dagan BVC-700A amplifier.

Borosilicate glass electrodes with electrode tip resistance between 3 and 7 megohms were pulled (P-97 Flaming/Brown micropipette puller; Sutter) from thick glass capillaries (1.5-mm outer diameter and 0.86-mm inner diameter; Sutter) and used for patch-clamp recordings. The pipette solution contained 120 mM K-gluconate, 20 mM KCl, 10 mM Hepes, 4 mM NaCl, 4 mM Mg–adenosine 5′-triphosphate, 0.3 mM Na–guanosine 5′-triphosphate, and 7 mM K_2-phosphocreatine (pH 7.3 adjusted with KOH; osmolarity ~300 mOsm). Series resistance was monitored and compensated online with the bridge-balance circuit of the amplifier. Experiments were discarded only if the initial resting membrane potential was more depolarized than −60 mV, if series resistance rose above 50 megohms, or if there were fluctuations in temperature and ACSF flow rate during the experiment. Voltages have not been corrected for the liquid junction potential, which was experimentally measured to be ~8 mV. Neuronal response to a 50-pA hyperpolarizing current pulse was continuously monitored to observe and correct series resistance changes using the bridge balance circuit throughout the experiment.

Pharmacological blockers

All recordings were performed in the presence of synaptic receptor blockers in the ACSF. Drugs and their concentrations used in the experiments were 10 μM 6-cyano-7-nitroquinoxaline-2, 3-dione, an AMPA receptor blocker; 10 μM (+) bicuculline and 10 μM picrotoxin, both $GABA_A$ receptor blockers; and 2 μM CGP55845, a $GABA_B$ receptor blocker (all synaptic blockers from Abcam) in the ACSF.

Subthreshold measurements

We characterized S1 pyramidal neurons with several electrophysiological measurements using standard protocols (*44*–*46*, *51*, *52*), detailed below. Resting membrane potential (V_{RMP}) was measured as the voltage at which the cell rested when no current was injected (figs. S3 and S4). Input resistance (R_{in}) was measured as the slope of a linear fit to the steady-state voltage-current (*V-I*) plot obtained by injecting subthreshold current pulses of amplitudes spanning −50 to 0 pA in steps of 10 pA (Fig. 2, A to D). The sag ratio was measured from the voltage response of the cell to a hyperpolarizing current pulse (figs. S3 and S4). Sag ratio was defined as ($V_{initial}$ / V_{SS}), where V_{SS} and $V_{initial}$ depict the steady-state and peak (during the initial 50-ms period after current injection) voltage deflections (from V_{RMP}), respectively. To assess temporal summation, five alpha excitatory postsynaptic potentials (α-EPSPs) with 50-ms intervals were injected as currents of the form $I_\alpha = I_{max} t \exp(-\alpha t)$, with $\alpha = 0.1\ ms^{-1}$. The temporal summation ratio (S_α) in this train of five EPSPs (figs. S3 and S4) was computed as E_{last}/E_{first}, where E_{last}, and E_{first} were the amplitudes of the last and first EPSPs in the train, respectively.

The chirp stimulus, a sinusoidal current with its frequency linearly spanning 0 to 15 Hz in 15 s and of constant amplitude adjusted to be below the firing threshold, was used to characterize the impedance profiles (figs. S3 and S4). The voltage response of the neuron was recorded for chirp current stimulus injection at V_{RMP}. The ratio of the Fourier transform of the voltage response to the Fourier transform of the chirp stimulus formed the impedance profile. The frequency at which the impedance amplitude reached its maximum was the resonance frequency (f_R). Resonance strength (Q) was measured as the ratio of the maximum impedance amplitude to the impedance amplitude at 0.5 Hz. The total inductive phase (Φ_L) was defined as the area under the inductive part of the impedance phase profile as a function of frequency (figs. S3 and S4).

Suprathreshold measurements

Action potential (AP) firing frequency was computed by extrapolating the number of spikes obtained during a 700-ms current injection to 1 s. The amplitude of these pulse current injections was varied from 0 to 250 pA in steps of 50 pA to construct the firing frequency vs injected current (*f-I*) plot (Fig. 2, E to H). In addition, to assess firing at higher current injections, we constructed *f-I* plots with high current injections ranging from 250 to 1250 pA in steps of 250 pA (fig. S5, C and D). Various AP-related measurements (*44*–*46*, *51*, *52*) were derived from the first action potential in the voltage response of the cell, resting at V_{RMP}, to a 500-pA pulse current injection (figs. S6 and S7). AP amplitude (V_{AP}) was computed as the difference between the peak voltage of the spike (V_{peak}) and V_{RMP} (figs. S6 and S7). The temporal distance between the timing of the first spike and the time of the current injection was defined as latency to the first spike T_{1AP} (figs. S6 and S7). The duration between the first and the second spikes was defined as the first interspike interval (figs. S6 and S7). AP half-width (T_{APHW}) was the temporal width measured at the half-maximal points of the AP peak concerning V_{RMP}. The maximum and minimum rate of change of voltage (dV/dt) of the AP temporal derivatives was calculated from the temporal first derivative of the voltage trace (figs. S6 and S7). The voltage in the AP trace corresponds to the time point at which the dV/dt crossed 20 V/s is defined as the AP threshold V_{th} (figs. S6 and S7).

Analyses of electrophysiological data and statistics

All data acquisition and analyses were performed with custom-written software in IGOR Pro (WaveMetrics), and statistical analyses were performed using the Wilcoxon rank sum test in the R computing package (www.r-project.org/).

Supplementary Materials

The PDF file includes:

Figs. S1 to S10

Legends for datasets S1 to S3

Other Supplementary Material for this manuscript includes the following:

Datasets S1 to S3

REFERENCES AND NOTES

1. K. L. Whitford, P. Dijkhuizen, F. Polleux, A. Ghosh, Molecular control of cortical dendrite development. *Annu. Rev. Neurosci.* **25**, 127–149 (2002).
2. W. E. Kaufmann, H. W. Moser, Dendritic anomalies in disorders associated with mental retardation. *Cereb. Cortex* **10**, 981–991 (2000).
3. V. A. Kulkarni, B. L. Firestein, The dendritic tree and brain disorders. *Mol. Cell. Neurosci.* **50**, 10–20 (2012).
4. S. Anderson, P. Vanderhaeghen, Cortical neurogenesis from pluripotent stem cells: Complexity emerging from simplicity. *Curr. Opin. Neurobiol.* **27**, 151–157 (2014).
5. J. Arikkath, Molecular mechanisms of dendrite morphogenesis. *Front. Cell. Neurosci.* **6**, 61 (2012).
6. J. L. Lefebvre, Molecular mechanisms that mediate dendrite morphogenesis. *Curr. Top. Dev. Biol.* **142**, 233–282 (2021).
7. R. F. Hevner, From radial glia to pyramidal-projection neuron: Transcription factor cascades in cerebral cortex development. *Mol. Neurobiol.* **33**, 33–50 (2006).
8. B. Cubelos, A. Sebastián-Serrano, L. Beccari, M. E. Calcagnotto, E. Cisneros, S. Kim, A. Dopazo, M. Alvarez-Dolado, J. M. Redondo, P. Bovolenta, C. A. Walsh, M. Nieto, Cux1 and Cux2 regulate dendritic branching, spine morphology, and synapses of the upper layer neurons of the cortex. *Neuron* **66**, 523–535 (2010).
9. B. Cubelos, C. G. Briz, G. M. Esteban-Ortega, M. Nieto, Cux1 and Cux2 selectively target basal and apical dendritic compartments of layer II-III cortical neurons. *Dev. Neurobiol.* **75**, 163–172 (2015).
10. S. Chiola, M. D. Do, L. Centrone, A. Mallamaci, Foxg1 overexpression in neocortical pyramids stimulates dendrite elongation via Hes1 and pCreb1 upregulation. *Cereb. Cortex* **29**, 1006–1019 (2019).
11. J.-G. Chen, M.-R. Rasin, K. Y. Kwan, N. Sestan, Zfp312 is required for subcortical axonal projections and dendritic morphology of deep-layer pyramidal neurons of the cerebral cortex. *Proc. Natl. Acad. Sci. U.S.A.* **102**, 17792–17797 (2005).
12. B. Yu, J. Liu, M. Su, C. Wang, H. Chen, C. Zhao, Disruption of Foxg1 impairs neural plasticity leading to social and cognitive behavioral defects. *Mol. Brain* **12**, 63 (2019).
13. R. Hand, D. Bortone, P. Mattar, L. Nguyen, J. I.-T. Heng, S. Guerrier, E. Boutt, E. Peters, A. P. Barnes, C. Parras, C. Schuurmans, F. Guillemot, F. Polleux, Phosphorylation of Neurogenin2 specifies the migration properties and the dendritic morphology of pyramidal neurons in the neocortex. *Neuron* **48**, 45–62 (2005).
14. Y. Hoshiba, T. Toda, H. Ebisu, M. Wakimoto, S. Yanagi, H. Kawasaki, Sox11 balances dendritic morphogenesis with neuronal migration in the developing cerebral cortex. *J. Neurosci.* **36**, 5775–5784 (2016).
15. I. Crespo, J. Pignatelli, V. Kinare, H. R. Méndez-Gómez, M. Esgleas, M. J. Román, J. M. Canals, S. Tole, C. Vicario, Tbr1 misexpression alters neuronal development in the cerebral cortex. *Mol. Neurobiol.* **59**, 5750–5765 (2022).
16. P.-S. Hou, D. Ó hAilín, T. Vogel, C. Hanashima, Transcription and beyond: Delineating FOXG1 function in cortical development and disorders. *Front. Cell. Neurosci.* **14**, 35 (2020).
17. A. S. Shetty, G. Godbole, U. Maheshwari, H. Padmanabhan, R. Chaudhary, B. Muralidharan, P.-S. Hou, E. S. Monuki, H.-C. Kuo, V. Rema, S. Tole, Lhx2 regulates a cortex-specific mechanism for barrel formation. *Proc. Natl. Acad. Sci. U.S.A.* **110**, E4913–E4921 (2013).
18. S. Pal, D. Dwivedi, T. Pramanik, G. Godbole, T. Iwasato, D. Jabaudon, U. S. Bhalla, S. Tole, An early cortical progenitor-specific mechanism regulates thalamocortical innervation. *J. Neurosci.* **41**, 6822–6835 (2021).
19. V. Lakhina, A. Falnikar, L. Bhatnagar, S. Tole, Early thalamocortical tract guidance and topographic sorting of thalamic projections requires LIM-homeodomain gene Lhx2. *Dev. Biol.* **306**, 703–713 (2007).
20. S. Goebbels, I. Bormuth, U. Bode, O. Hermanson, M. H. Schwab, K.-A. Nave, Genetic targeting of principal neurons in neocortex and hippocampus of NEX-Cre mice. *Genesis* **44**, 611–621 (2006).
21. G. A. Chinn, K. E. Hirokawa, T. M. Chuang, C. Urbina, F. Patel, J. Fong, N. Funatsu, E. S. Monuki, Agenesis of the corpus callosum due to defective glial wedge formation in lhx2 mutant mice. *Cereb. Cortex* **25**, 2707–2718 (2015).
22. H. Hering, M. Sheng, Dendritic spines: Structure, dynamics and regulation. *Nat. Rev. Neurosci.* **2**, 880–888 (2001).
23. L. H.-Y. Lo, K.-O. Lai, Dysregulation of protein synthesis and dendritic spine morphogenesis in ASD: Studies in human pluripotent stem cells. *Mol. Autism.* **11**, 40 (2020).
24. J. F. Costa, M. Dines, R. Lamprecht, The role of rac gtpase in dendritic spine morphogenesis and memory. *Front. Synaptic Neurosci.* **12**, 12 (2020).
25. A. Matus, Growth of dendritic spines: A continuing story. *Curr. Opin. Neurobiol.* **15**, 67–72 (2005).
26. Z. F. Mainen, T. J. Sejnowski, Influence of dendritic structure on firing pattern in model neocortical neurons. *Nature* **382**, 363–366 (1996).
27. R. Narayanan, S. Chattarji, Computational analysis of the impact of chronic stress on intrinsic and synaptic excitability in the hippocampus. *J. Neurophysiol.* **103**, 3070–3083 (2010).
28. D. J. Di Bella, E. Habibi, R. R. Stickels, G. Scalia, J. Brown, P. Yadollahpour, S. M. Yang, C. Abbate, T. Biancalani, E. Z. Macosko, F. Chen, A. Regev, P. Arlotta, Molecular logic of cellular diversification in the mouse cerebral cortex. *Nature* **595**, 554–559 (2021).
29. A. Kawaguchi, M. Ogawa, K. Saito, F. Matsuzaki, H. Okano, T. Miyata, Differential expression of Pax6 and Ngn2 between pair-generated cortical neurons. *J. Neurosci. Res.* **78**, 784–795 (2004).
30. Z. Li, W. A. Tyler, E. Zeldich, G. Santpere Baró, M. Okamoto, T. Gao, M. Li, N. Sestan, T. F. Haydar, Transcriptional priming as a conserved mechanism of lineage diversification in the developing mouse and human neocortex. *Sci. Adv.* **6**, eabd2068 (2020).
31. K. Oishi, D. L. C. van den Berg, F. Guillemot, Temporal control of cortico-thalamic neuron specification by regulation of Neurogenin activity and Polycomb repressive complexes. *BioRxiv* (2018), doi:10.1101/431684.
32. R. G. Morgan, J. Ridsdale, A. Tonks, R. L. Darley, Factors affecting the nuclear localization of β-catenin in normal and malignant tissue. *J. Cell. Biochem.* **115**, 1351–1361 (2014).
33. A. Parichha, V. Suresh, M. Chatterjee, A. Kshirsagar, L. Ben-Reuven, T. Olender, M. M. Taketo, V. Radosevic, M. Bobic-Rasonja, S. Trnski, M. J. Holtzman, N. Jovanov-Milosevic, O. Reiner, S. Tole, Constitutive activation of canonical Wnt signaling disrupts choroid plexus epithelial fate. *Nat. Commun.* **13**, 633 (2022).
34. A. Chenn, Wnt/β-catenin signaling in cerebral cortical development. *Organogenesis* **4**, 76–80 (2008).
35. F. Noack, S. Vangelisti, G. Raffl, M. Carido, J. Diwakar, F. Chong, B. Bonev, Multimodal profiling of the transcriptional regulatory landscape of the developing mouse cortex identifies Neurog2 as a key epigenome remodeler. *Nat. Neurosci.* **25**, 154–167 (2022).
36. R. Hand, F. Polleux, Neurogenin2 regulates the initial axon guidance of cortical pyramidal neurons projecting medially to the corpus callosum. *Neural Dev.* **6**, 30 (2011).
37. A. J. Hulme, S. Maksour, M. St-Clair Glover, S. Miellet, M. Dottori, Making neurons, made easy: The use of Neurogenin-2 in neuronal differentiation. *Stem Cell Rep.* **17**, 14–34 (2022).
38. S. B. Rosso, N. C. Inestrosa, WNT signaling in neuronal maturation and synaptogenesis. *Front. Cell. Neurosci.* **7**, 103 (2013).
39. B. Muralidharan, Z. Khatri, U. Maheshwari, R. Gupta, B. Roy, S. J. Pradhan, K. Karmodiya, H. Padmanabhan, A. S. Shetty, C. Balaji, U. Kolthur-Seetharam, J. D. Macklis, S. Galande, S. Tole, LHX2 interacts with the NuRD complex and regulates cortical neuron subtype determinants Fezf2 and Sox11. *J. Neurosci.* **37**, 194–203 (2017).
40. C.-W. He, C.-P. Liao, C.-L. Pan, Wnt signalling in the development of axon, dendrites and synapses. *Open Biol.* **8**, 180116 (2018).
41. X. Yu, R. C. Malenka, β-catenin is critical for dendritic morphogenesis. *Nat. Neurosci.* **6**, 1169–1177 (2003).
42. B. Viale, L. Song, V. Petrenko, A.-L. Wenger Combremont, A. Contestabile, R. Bocchi, P. Salmon, A. Carleton, L. An, L. Vutskits, J. Z. Kiss, Transient deregulation of canonical wnt signaling in developing pyramidal neurons leads to dendritic defects and impaired behavior. *Cell Rep.* **27**, 1487–1502.e6 (2019).
43. C. M. Schmid, A. Gregor, G. Costain, C. F. Morel, L. Massingham, J. Schwab, C. Quélin, M. Faoucher, J. Kaplan, R. Procopio, C. J. Saunders, A. S. A. Cohen, G. Lemire, S. Sacharow, A. O'Donnell-Luria, R. J. Segal, J. Kianmahd Shamshoni, D. Schweitzer, D. Ebrahimi-Fakhari, K. Monaghan, C. Zweier, LHX2 haploinsufficiency causes a variable neurodevelopmental disorder. *Genet. Med.* **25**, 100839 (2023).
44. S. Ashhad, R. Narayanan, Active dendrites regulate the impact of gliotransmission on rat hippocampal pyramidal neurons. *Proc. Natl. Acad. Sci. U.S.A.* **113**, E3280–E3289 (2016).
45. P. Mishra, R. Narayanan, Heterogeneities in intrinsic excitability and frequency-dependent response properties of granule cells across the blades of the rat dentate gyrus. *J. Neurophysiol.* **123**, 755–772 (2020).
46. P. Mishra, R. Narayanan, Conjunctive changes in multiple ion channels mediate activity-dependent intrinsic plasticity in hippocampal granule cells. *iScience* **25**, 103922 (2022).
47. T. Kohno, T. Honda, K.-I. Kubo, Y. Nakano, A. Tsuchiya, T. Murakami, H. Banno, K. Nakajima, M. Hattori, Importance of Reelin C-terminal region in the development and maintenance of the postnatal cerebral cortex and its regulation by specific proteolysis. *J. Neurosci.* **35**, 4776–4787 (2015).
48. D. Kim, J. M. Paggi, C. Park, C. Bennett, S. L. Salzberg, Graph-based genome alignment and genotyping with HISAT2 and HISAT-genotype. *Nat. Biotechnol.* **37**, 907–915 (2019).
49. M. I. Love, W. Huber, S. Anders, Moderated estimation of fold change and dispersion for RNA-seq data with DESeq2. *Genome Biol.* **15**, 550 (2014).
50. S. X. Ge, D. Jung, R. Yao, ShinyGO: A graphical gene-set enrichment tool for animals and plants. *Bioinformatics* **36**, 2628–2629 (2020).
51. R. Narayanan, D. Johnston, The h channel mediates location dependence and plasticity of intrinsic phase response in rat hippocampal neurons. *J. Neurosci.* **28**, 5846–5860 (2008).
52. R. Narayanan, D. Johnston, Long-term potentiation in rat hippocampal neurons is accompanied by spatially widespread changes in intrinsic oscillatory dynamics and excitability. *Neuron* **56**, 1061–1075 (2007).

Acknowledgments: We thank S. Suryavanshi and the animal house staff of the Tata Institute of Fundamental Research (TIFR) for their excellent support; E. Monuki for the *Lhx2* floxed

mouse line; M. M. Taketo (Kyoto University, Japan) for the *Ctnnb1* exon-3 floxed line; M. Sonawane (Tata Institute of Fundamental Research, India) for the CAAX-*Egfp* and CAAX-*mCherry* plasmids; T. Haydar (University of Maryland, USA) for the *Eomes*-Cre plasmid; and F. Guillemot (Francis Crick Institute, London, UK) for the pSilcaggs-*Neurog2*-shRNA-EGFP and pSilcaggs-scrambled-EGFP plasmids. We thank Medgenome Inc. for sequencing the RNA libraries. We thank V. Suresh for assistance with the initial processing of the RNA-seq data. **Funding:** This work was funded by the Department of Atomic Energy (DAE), Govt. of India (project identification no. RTI4003, DAE OM no. 1303/2/2019/R&D-II/DAE/2079) (S.T.). **Author contributions:** Conceptualization: M.B. and S.T. Formal analysis: M.B., S.R., S.K., R.N., and A.S. Methodology: M.B., S.R., S.K., and R.N. Investigation: M.B., S.R., S.K., A.I., B.V., A.S., and I.T. Visualization: M.B., S.R., A.S., S.K., and R.N. Supervision: S.T. and R.N. Writing–original draft: M.B., S.K., and R.N. Writing–review and editing: M.B., S.K., R.N., and ST. **Competing interests:** The authors declare that they have no competing interests. **Data and materials availability:** All data needed to evaluate the conclusions in the paper are present in the paper. Raw and processed data of RNA-seq are available at NCBI GEO: GSE253914.

Submitted 25 January 2024
Accepted 27 May 2025
Published 2 July 2025
10.1126/sciadv.ado1384